Paper: ASAT-17-127-PP

17th International Conference on
AEROSPACE SCIENCES & AVIATION TECHNOLOGY,
ASAT - 17 – April 11 - 13, 2017, E-Mail: asat@mtc.edu.eg
Military Technical College, Kobry Elkobbah, Cairo, Egypt
Tel: +(202) 24025292 – 24036138, Fax: +(202) 22621908

The Influence of Turbulence Modeling Technique on Centrifugal Pump Simulation

{S. M. Selim, M. A. Hosien, S. M. El-Behery* and M. Elsherbiny}†

Abstract: This paper presents a comparative study on the performance of different turbulence models for simulating the internal flow in a centrifugal pump. The models either depend on Boussinesq hypothesis or solve separate equation for each turbulence stress. These models include Reynolds stress model (RSM) Three dimensional unsteady RANS equations are solved. The effect of predicted turbulence quantity on the most unsteady parameter inside the pump (impeller-volute interaction) is performed using sliding mesh technique. The numerical results at different position within the pump are compared with experimental form literature. The experimental results of radial and relative tangential velocity were obtained using Laser Doppler Velocimeter (LDV). Although each turbulence model indicates some physical phenomena which cannot be predicted by the others, the standard k-ε model proves quantitatively its ability to perform this task. This conclusion is deduced from the analysis of the mean deviation error for all tested models. Moreover, some physical phenomena inside the pump are analyzed.

Keywords: Centrifugal pump; Turbulence models; Sliding mesh; Unsteady flow

1. Introduction

The centrifugal pumps are used in many engineering applications for fluid transportation. Therefore, a large number of studies had been carried out to improve the pump performance. Due to the complexity of centrifugal pump geometry, it is very difficult to measure experimentally the detailed characteristics of flow inside the pump. In the last few decades the computer power and numerical techniques had been improved significantly. As A result, the simulation of unsteady turbulent flow inside the centrifugal pump becomes available. Various commercial codes (FLUENT, CFX-Tascflow, STAR-CD and FINE/Turbo) prove their ability to carry out such simulation. Selim *et al.* [1] simulated the flow through centrifugal pump using 2D technique. Their results showed that some physical phenomena inside the pump were not captured accurately. González *et al.* [2], Mentzos *et al.* [3], Barrio *et al.* [4] and Silva *et al.* [5] performed 3D simulation of turbulent flow inside the pump. The turbulence modeling is a key issue in most of the previous research. Selim *et al.* [1] and Nocente *et al.* [6] indicated that the realizable k-ε is better than other turbulence models. While Chakraborty and Pandey [7], González *et al.*[2], Barrio *et al.* [4] used the standard k-ε in their simulation. Moreover, Yulin *et al*. [8] and Liu *et al.* [9] indicated that, the SST k-ω is more suitable for centrifugal pump simulation. Even the one equation turbulence model (Spalart-Allmaras) was chosen by Silva *et*

* Email: s_elbehery@yahoo.com, Tel.: +201008002457
† Mechanical Power Engineering Department, Faculty of Engineering, Menoufyia University, Shebin El-Kom, Egypt.

al. [5] and Westra *et al.*[10]. Therefore, there is no universal turbulent model can be adopted from the previous studies for centrifugal pump simulation [11].

In this paper, realizable k-ε, standard k-ε, RSM and SST k-ω turbulence models are used to predict the velocity components inside centrifugal pump. The numerical results for all models are compared with experimental data reported by Miner *et al.* [12].

2. Mathematical Modeling

Centrifugal pump has moving (impeller) and fixed (inlet pipe, volute and exit pipe) domains. The fluid in both domains can be solved without impeller rotation by representing the equations of each domain to co-ordinate moves at the same speed of each one (Multi Reference frame). Another modelling approach deals with the unsteady solution (Sliding mesh technique). In this approach, the equation of both domains is represented to generalize, stationary co-ordinate. Therefore, the impeller-volute interaction and impeller rotation are considered. The discretization procedure of the governing equations is accomplished by ANSYS FLUENT 15 [13]. The instantaneous variables are substituted by the average and fluctuating components. After that, the time average is taken for all equations. This technique is knowing as Reynolds average Navier-Stocks technique. RANS technique is considered the most practical one as it consumes low time in calculation procedure.

2.1 Governing Equations

The fluid flows through the pump can be considered as 3D, Newtonian, incompressible and isothermal. The governing equations for all models (MRF or SMM) can be generalized in absolute velocity formulation and Cartesian tensor as follow:

$$\frac{\partial}{\partial x_i}(W_{ri}) = 0 \tag{1}$$

$$\rho\left(\frac{\partial}{\partial t}(u_i) + \frac{\partial}{\partial x_j}(u_i W_{rj})\right) = -\frac{\partial p}{\partial x_i} + \frac{\partial}{\partial x_j}\left[\mu\left(\frac{\partial u_i}{\partial x_j}\right)\right] + \rho\frac{\partial}{\partial x_j}(-\overline{u_i' u_j'}) - \rho\Gamma\left[e_{ijK}\Omega_i u_k\right] + S_{p_i} \tag{2}$$

$$u_i = W_{ri} + e_{ijK}\Omega_i r_K \tag{3}$$

where W_{ri} is the average relative velocity,is known as Ω_i ity,is the average absolute veloc u_i the angular speed, S_{p_i} represents the momentum exchange source term Γ is a blinding functio

The equations represent the inertial frame when the value of angular speed is zero ($\Omega_i = 0$).

- If $\Gamma = 0$, it represents the governing equations for sliding mesh technique.
- If $\Gamma = 1$, it represents the governing equations for multi reference frame at which the Coriolis and centrifugal acceleration can be introduced in term of $\rho e_{ijK}\Omega_i u_k$.

e_{ijK} is alternative unit tensor and evaluated as

- $e_{ijK} = 0$ if any two indices are equal.
- $e_{ijK} = +1$ if the indices form an even permutation of 123.
- $e_{ijK} = -1$ if the indices form an odd permutation of 123.

Equation (2) has a new term known as Reynolds-stress tensors $\rho\overline{u_i' u_j'}$. In order to close the governing equations, additional relations should be added. Consequently, the concept of various turbulence models is introduced. Some of turbulence models produce separate equation for each Reynold stress (Reynold stress model) and another depend on Boussinesq hypothesis.

2.2 Reynold Stress Model (RSM)

It is considered more suitable for anisotropic of the Reynolds stress applications, complex flow, streamlines curvature, swirl and rotation. Although the exact equation for each Reynolds stress is employed, the limitation of its predicted results is found. This limitation comes from the assumption employed in its equations. More description can be found in Ref. [14].

2.3 Boussinesq Approaches

Boussinesq hypothesis relates the Reynolds stresses with the gradient of mean velocity as follow:

$$-\rho\overline{u_i'u_j'} = \mu_t\left(\frac{\partial u_i}{\partial x_j}+\frac{\partial u_j}{\partial x_i}\right)-\frac{2}{3}(\rho k)\delta_{ij} \qquad (4)$$

The δ_{ij} is named as the Kronecker delta function where $\delta_{ij}=1 \text{ if } i=j$, $\delta_{ij}=0 \text{ if } i\neq j$ and k is turbulent kinetic energy.

A new parameter (μ_t known as turbulent viscosity) is introduced in equation (4). Several turbulence models such as standard k-ε model, realizable k-ε model and SST k-ω model are trying to represent this parameter.

Standard k-ε model

It was proposed by Launder and Spalding [15]. The turbulent viscosity μ_t is determined through calculating the turbulent kinetic energy (k) and its dissipation rate (ε). These terms are important on detecting the characteristics of turbulent eddies by calculating the turbulent length scale $\ell_s=\frac{k^{3/2}}{\varepsilon}$ and turbulent time scale $\tau_s=\frac{k}{\varepsilon}$. It becomes the general model in practical engineering as it takes lower calculation time and gives reasonable accuracy. It assumes that the flow is fully turbulent (turbulent viscosity is constant in each direction), also the effect of molecular viscosity is negligible.

Realizable k-ε model

The term "realizable" means that, the model satisfies certain mathematical constraints on Reynolds stresses according to the physics of turbulent flows. It was proposed by Shih *et al.* [16]. This model modifies the standard k-ε calculation procedure of two parameters (turbulent viscosity (μ_t) and dissipation rate (ε)). It contains alternative formulation for the turbulent viscosity.

Shear-stress transport (SST) k-ω model

Menter [17] who suggested this model, made blending between standard k-ω model, which gives a robust and accurate formulation in the near-wall region, with the free stream independence of the standard k-ε model in the far field. Standard k-ω depends on transport equations for turbulence kinetic energy k and specific dissipation rate ω which is defined as $\omega=\varepsilon/k$. The standard k-ω model introduces a modification for low- Reynolds number effect (near-wall flow).

3. Computational Domain and Boundary Condition

The physical domain consists of inlet pipe, impeller and volute casing. In order to simplify geometry and reduce the computational cost, the space between impeller faces and stationary housing is neglected. Moreover, the inlet pipe is shortened to about three times of pipe diameter. This length is ensured to be sufficient by calculating the pump geometry with inlet pipe of

length $l = 17D$. The flow is uniform at this section as reported by Miner *et al.* [12]. The velocity profiles at different sections upstream of the impeller, shown in Fig. 1, demonstrate the pump effect diminished at length of about $l = 3D$.

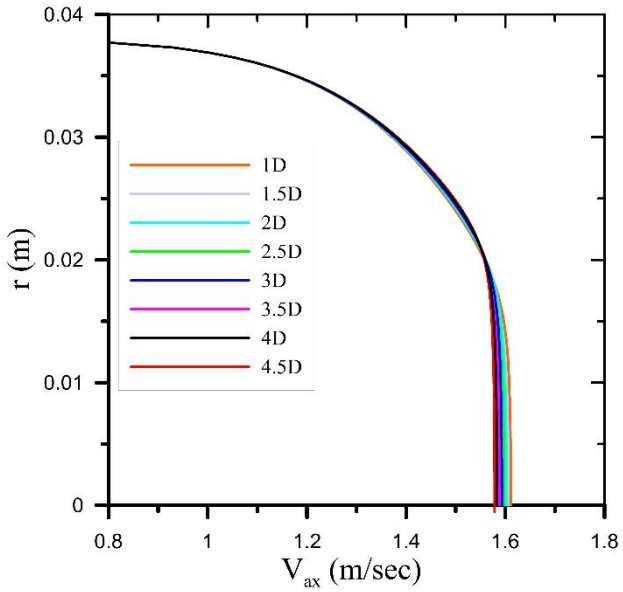

Fig. 1. Axial velocity profiles at different sections along the inlet pipe.

The 3D pump geometry is created by SolidWorks CAD program. The impeller blades are designed according to Thin *et al.* [18]. While the pump volute is set up according to the equation of its manufacturing $r = 108\, e^{0.115(\theta - 0.1145)}$. For grid generation, the pump geometry is divided into a large number of hexahedral structured computational mesh using ANSYS-Meshing 15. Therefore, each pump domain is divided into subdomains as shown in Fig. 2. The division is performed in a way that, the density and the quality of the cells in local flow field regions can be suitably controlled. The velocity and turbulent quantities profiles at the pump inlet are extracted from the fully developed flow of a pipe of sufficient length solving at the same pump flow rate. Constant pressure is adopted at the outlet of centrifugal pump. Also, no slip boundary condition is used at the solid walls. The faces between stationary and moving mesh, inlet-impeller and impeller-volute, are treated as interface zones. The boundary conditions for the pump simulation is illustrated in Fig. 3.

4. Solution Procedure

The transport equations are discretized using finite volume method with second order upwind scheme. The discretized equations are solved by a coupled algebraic method (coupled solution of mass and momentum). First, a converged solution is obtained using steady state, Multi Reference Frame (MRF) technique. This solution is used as initial gausses for the unsteady solution of Sliding Mesh Method (SMM). Before the numerical simulation is released, there are some parameters that must have neglected influence on the simulation. These parameters are grid and time step effect. Therefore, two tests (grid independence and time step) are made to determine the best value for both parameters. Firstly, different meshes with different characteristics, shown in Table 1, are examined. Figure 4 demonstrated that, the improvement in results performed by $mesh_3$ can be neglected compared with the high computational time associated with it. Therefore, it can be concluded that $mesh_2$ is the best mesh adopted for the following calculation.

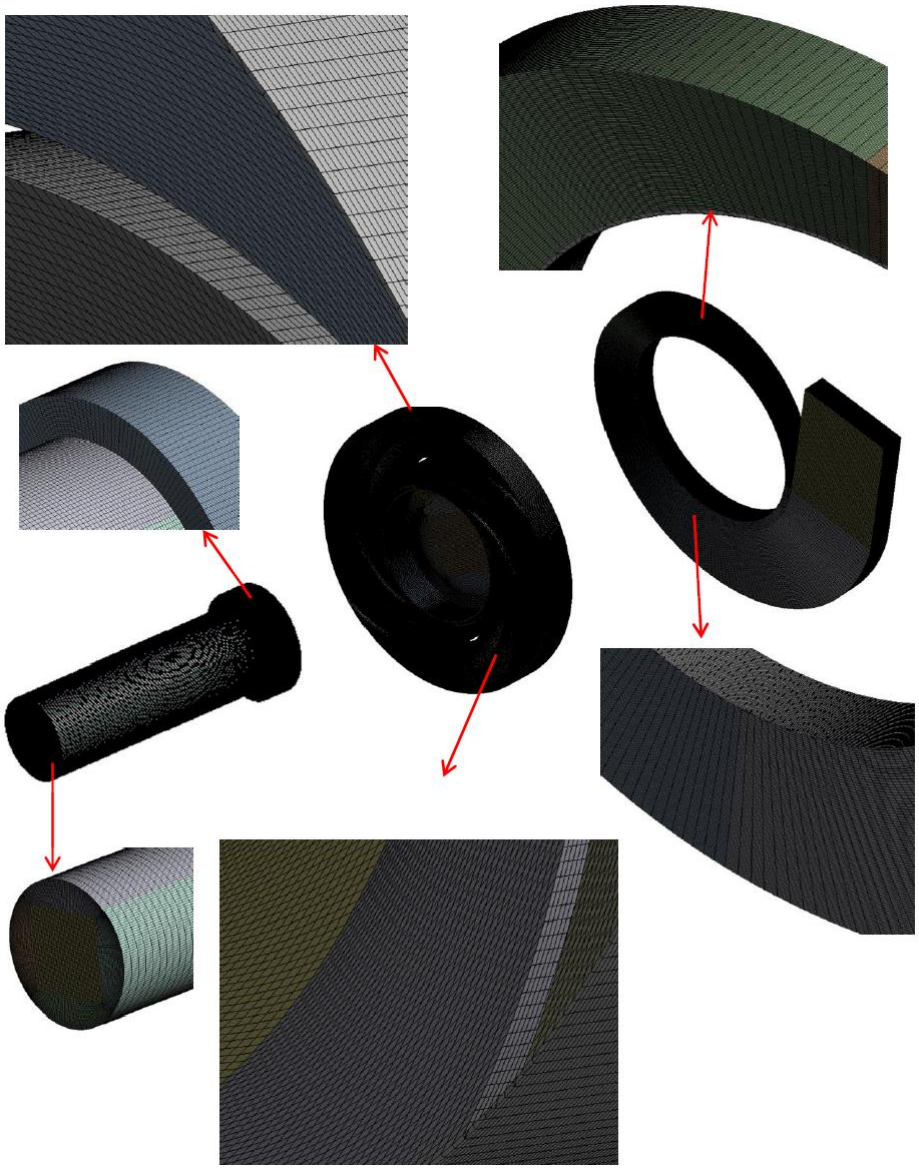

Fig. 2. Mesh of different centrifugal pump parts.

Table 1. Number of cells in each part for both pumps.

Pump part	$Mesh_1$	$Mesh_2$	$Mesh_3$
Inlet pipe	0.97×10^6	1.36×10^6	1.36×10^6
Impeller	3.45×10^6	4.70×10^6	7.285×10^6
Volute	1.57×10^6	2.074×10^6	3.214×10^6
Total	5.99×10^6	8.134×10^6	11.859×10^6
Wall y^+	$6.15 < y^+ < 138$	$1.73 < y^+ < 70$	$1.37 < y^+ < 67$

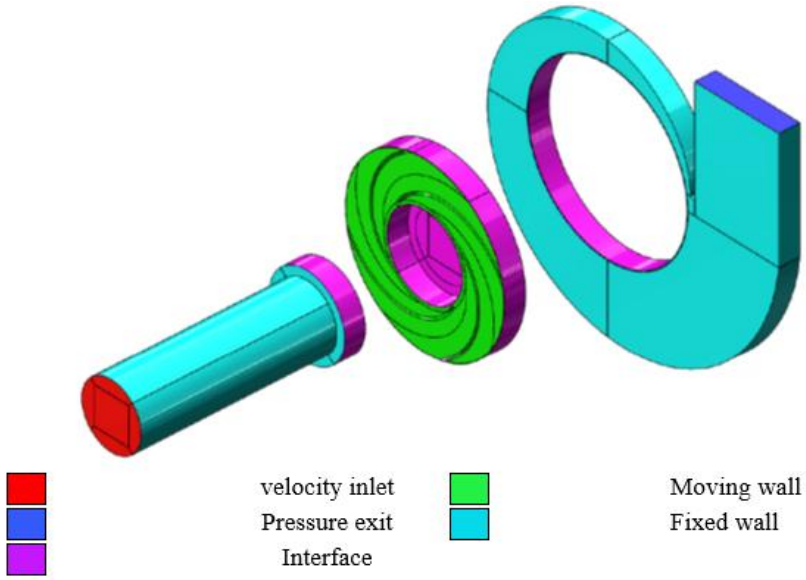

Fig. 3. Implementation of boundary conditions.

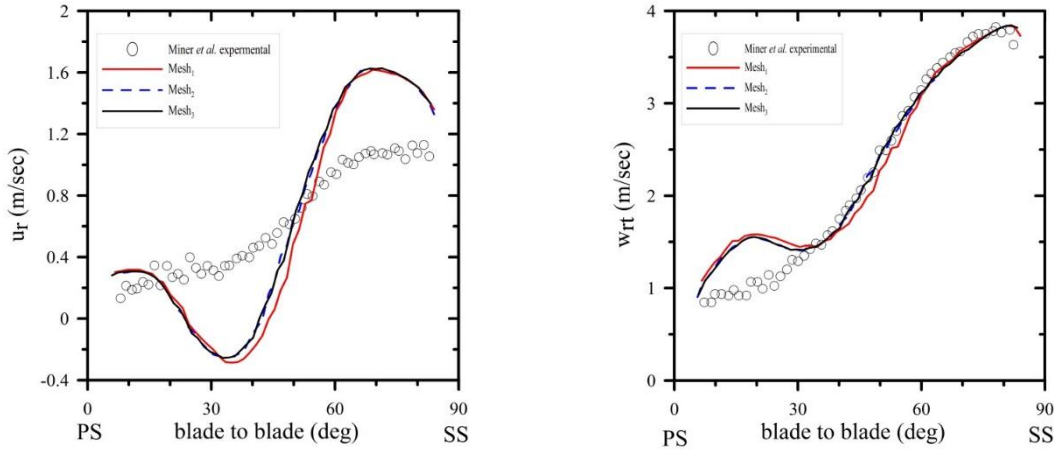

Fig. 4. Effect of grid size on radial and relative tangential velocity components

Concerning with the time step, the time step should be lower than the blade thickness time (4.6032×10^{-4}sec. for measured points at radius $r = 100.3mm$) to be recognized accurately of the blade passage frequency. Therefore, Computation of two time steps less than the blade thickness time is presented in Fig. 5. The results obtained with $\Delta t = 2 \times 10^{-4}$sec. and 4×10^{-4}sec. are very close. Therefore, $\Delta t = 4 \times 10^{-4}$sec. (represents impeller rotation of less than 1.5 degree in each time step) is selected in the present study.

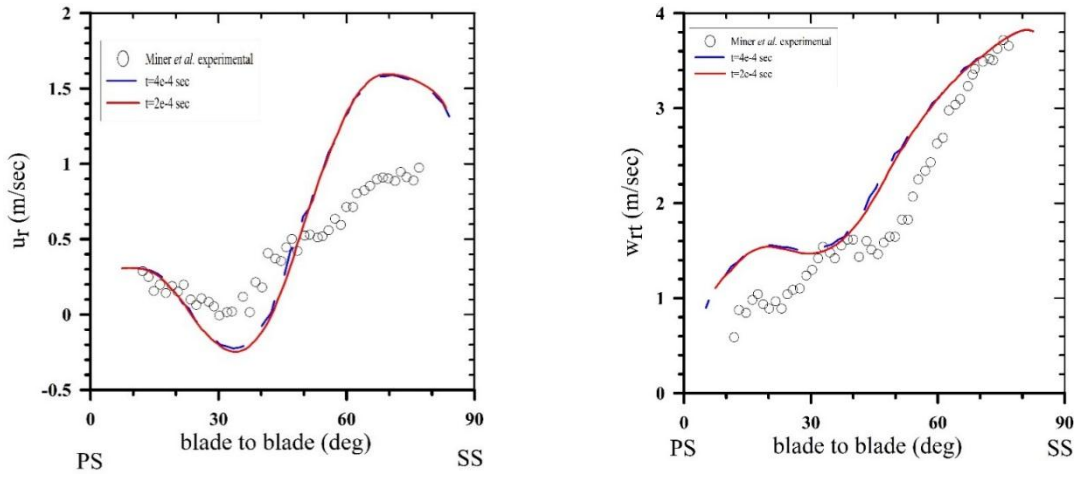

Fig. 5. Effect of time step on radial and relative tangential velocity components at $\boldsymbol{\theta = 0}$ and $\boldsymbol{r = 63.5\ mm}$

5. Results and Discussion

The measured and predicted values for radial and relative tangential velocity components for various turbulence models at $r = 63.5$ mm and $\theta = \pi$ and 0 are shown in Fig. 6. It can be seen from experimental results that; the radial and relative tangential velocities are lower at the pressure side than at the other side (suction side). The pressure side is the blade surface facing the flow in the direction of rotation as defined by Farge and Johnson [19], Abramian and Howard [20] and Selim *et al.* [1].

The difference in the value of the square relative velocity magnitude on both sides is caused by the pressure difference as governed by Rothalpy equation. The mathematical form for this equation can be written as $I = \frac{p}{\rho g} + \frac{W_r^2}{2g} - \frac{(\Omega r)^2}{2g} - losses$. Consequently, at the same impeller radius, when the static pressure head increases, the relative velocity magnitude decreases.
The pressure difference between the two sides of the blade (pressure and suction sides) is called Blade loading. The larger the pressure difference is, the larger the blade loading becomes. To explain this phenomenon, the predicted relative velocity and pressure are presented at different radii ($r = 60, 70, 80, 90, 100\ mm$) across the flow passages, as shown in Fig. 7. It is shown that the relative velocity on suction side is higher than pressure side. According to equivalence in energy acquired at the same elevation, the pressure value at pressure side is higher than suction side. The velocity difference between two surfaces decreases with increase of radius. Therefore, the blade loading decreases as illustrated in Fig. 8.

The major differences between the experimental results taken at both pervious points are the appearance of zero radial velocity at $\theta = 0$, the flowrate at both points isn't equal and a region of constant relative tangential velocity is also existed. It is the indication of asymmetry in flow field in the impeller passages even at design flowrate as reported by Hamkins and Flack [21] and Miner *et al.* [12]. The onset of inlet recirculation appears when the radial velocity becomes zero. Part of the entering flow turns around and flow back into the inlet pipe, as shown in Fig. 9. As the flow changes its direction from axial to radial, the flow becomes closer to the hub side. Also, the inlet flow angle (measured from plane of rotation) is larger than the blade angle. So, the separation occurs at the pressure side. This separation can be considered the seed of the inlet recirculation.

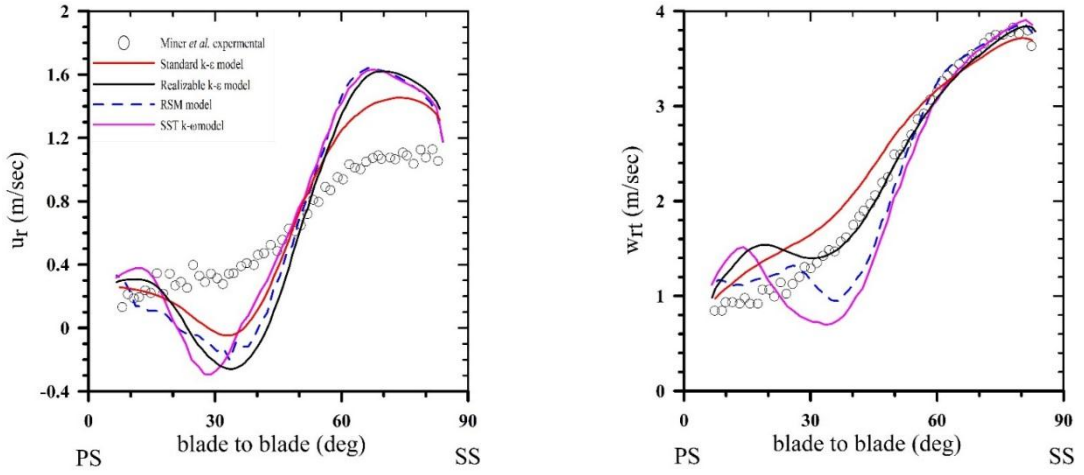

(a) $\theta = \pi$.

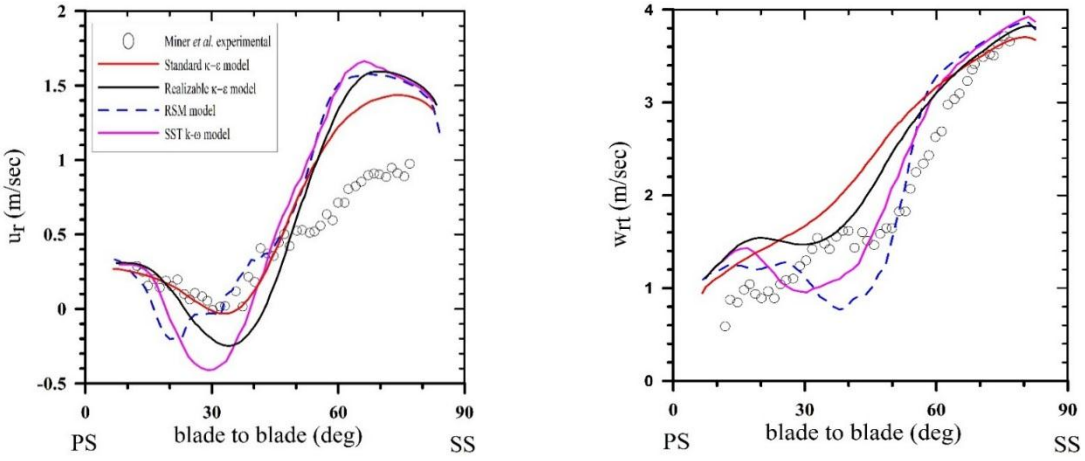

(b) $\theta = 0$.

Fig. 6. Radial and relative tangential velocity distribution at $\boldsymbol{r = 63.5}$ mm and $\boldsymbol{z = 12.3}$ mm.

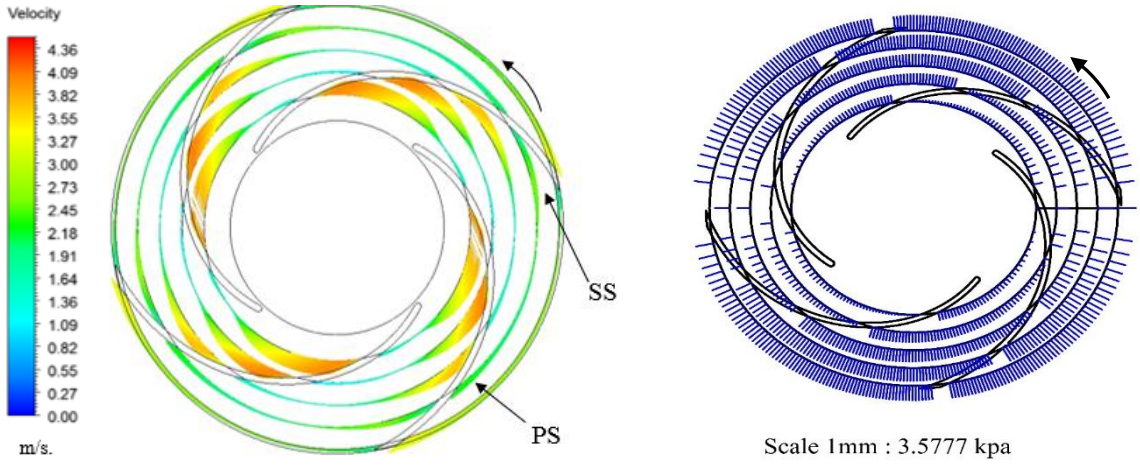

Fig. 7. Relative velocity and static pressure distribution in flow passages at different radii.

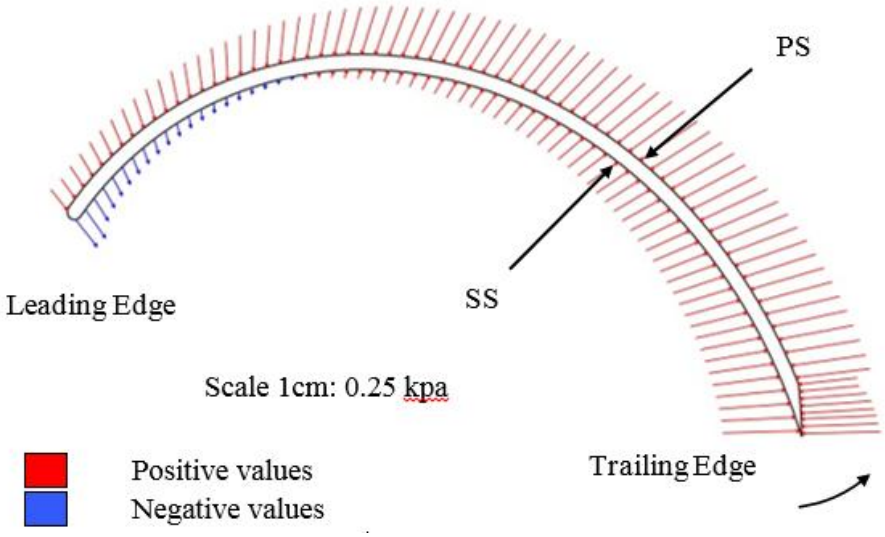

Fig. 8. Pressure distribution along blade surfaces.

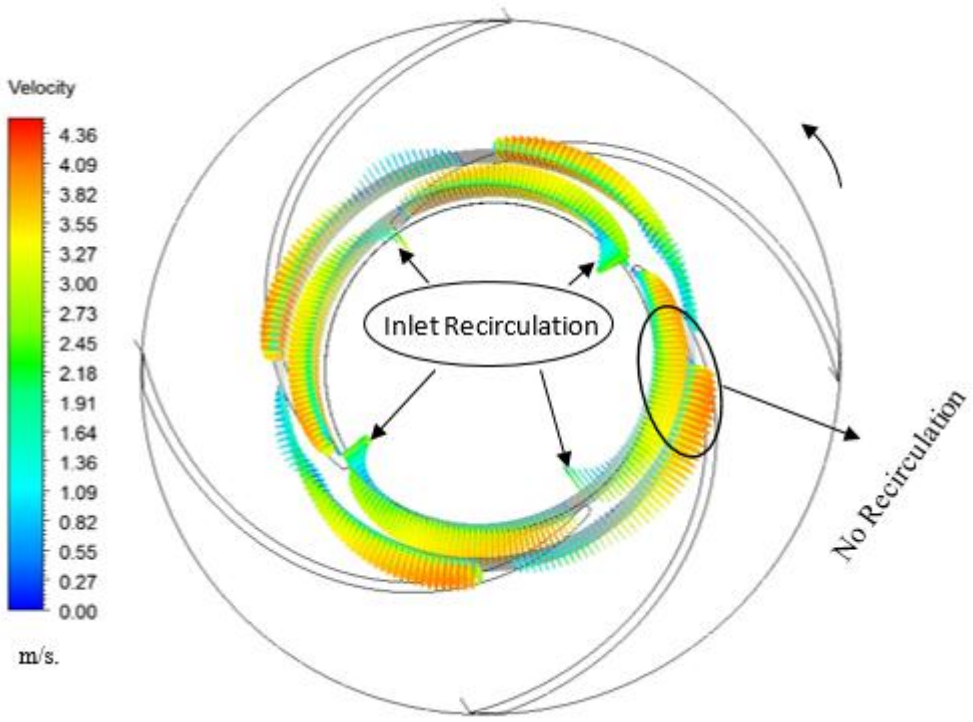

Fig. 9. Relative velocity distribution in axial direction.

While the numerical method predicts lower relative velocity components at the pressure side than its value at the suction side, the trend of predicted radial velocity doesn't similar to experimental as seen in Fig. 6-a, despite the area under both curves (flowrate) are approximately the same. The numerical results are over predicted at the suction side and under predicted in the other side. However, at Fig. 6-b, all turbulence models predict the same experimental trend with flowrate higher than that obtained experimentally. The numerical method fails to indicate this difference. It represents the recirculation happens in all passage whatever its position. The standard k-ε model can be considered as the best one for the radial velocity. The region that has constant relative tangential velocity is predicted only by realizable k-ε model.

The radial and relative tangential velocities at next radius $r = 88.9$ mm for both angles are shown in Fig. 10. The results in this figure display not only the decrease of blade loading but also, the decrease in radial velocity. The decrease in radial velocity magnitude occurs at approximately two-thirds blade passage from pressure side. Moreover, its magnitude at suction side is lower than the value acquired at previous measured radius. The indication for secondary flow which considers the main responsible for the variation in the flow with the pump thickness is confirmed. Pedersen *et al.* [24] reported that the decrease in radial velocity and the growth in relative tangential component, especially at pressure side, can be attributed to the gradual increase in the Coriolis force.

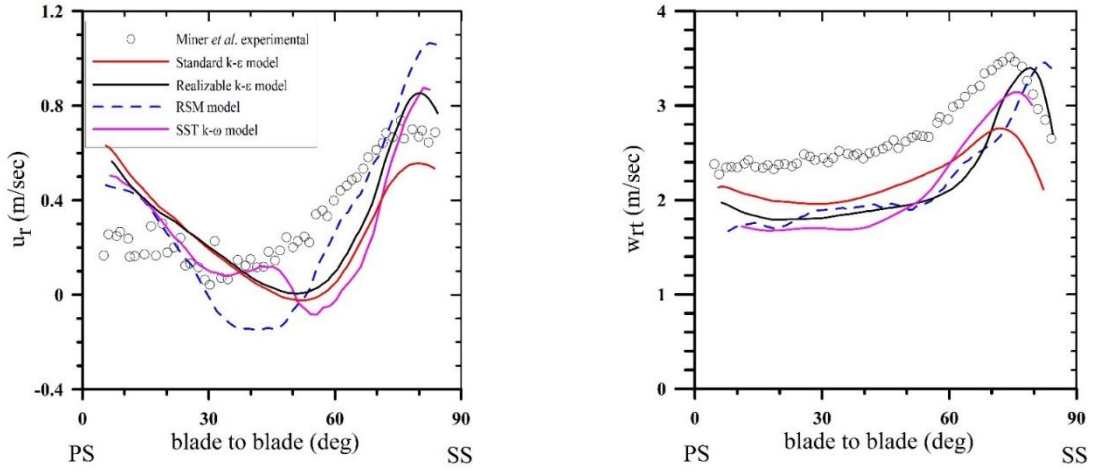

(a) $\theta = \pi$.

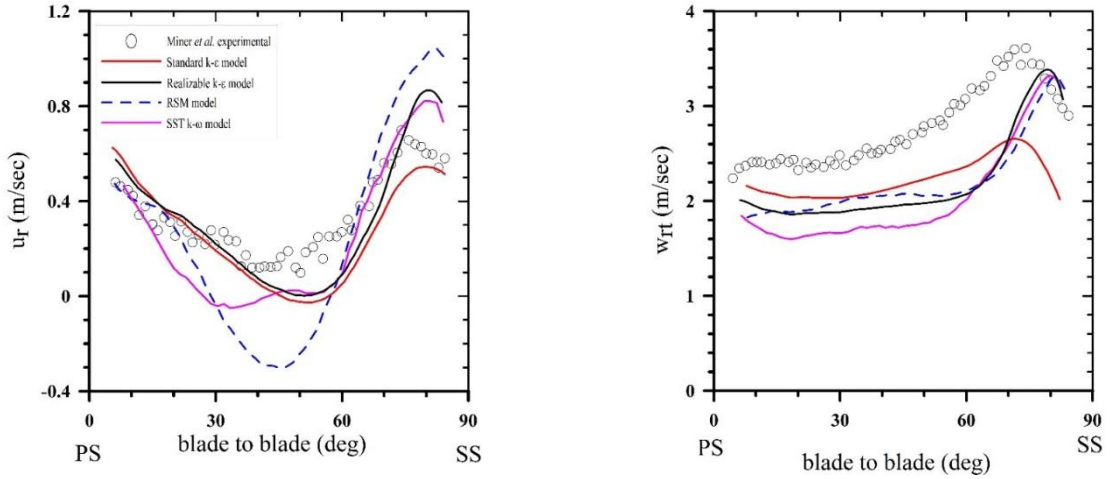

(b) $\theta = 0$.

Fig. 10. Radial and relative tangential velocity
at $\boldsymbol{r = 88.9}$ mm and $\boldsymbol{z = 12.3}$ mm.

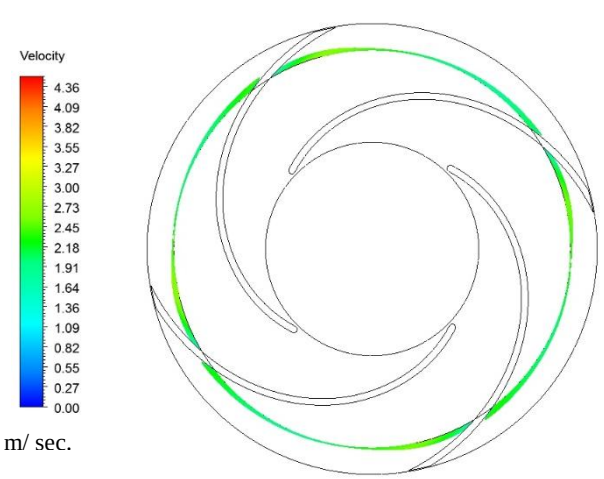

(a) Relative velocity at $r = 88.9$ mm.

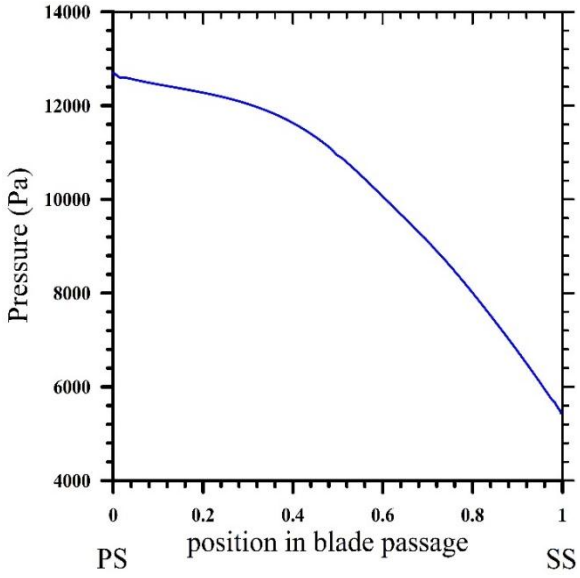

(b) Pressure distribution $r = 88.9$ mm.

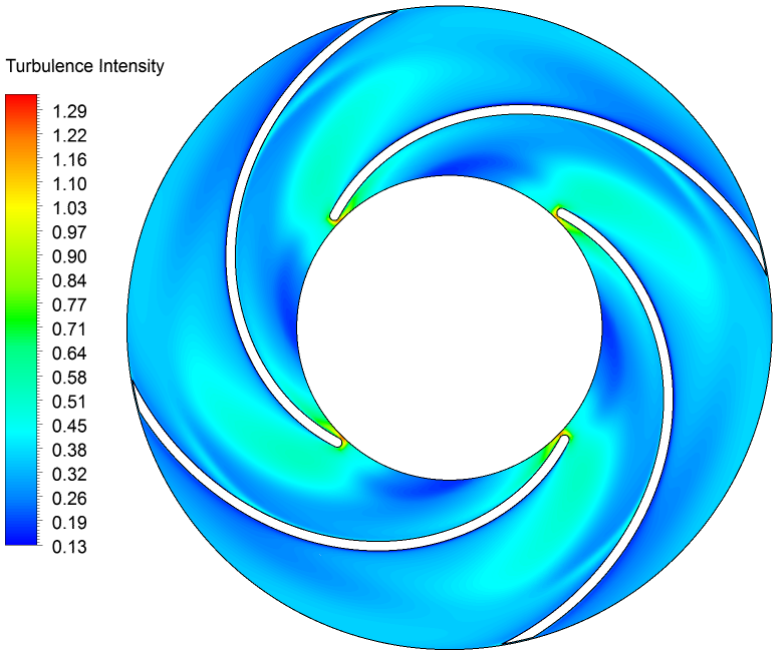

(c) Turbulence intensity in the whole impeller.

Fig. 11. Effect of Coriolis force on the flow characteristics.

The appearance of Coriolis force can be represented by a dimensionless number called Rossby number$Ro = \frac{W_r}{\Omega R_n}$ where R_n is the radius of curvature of impeller passage. According to its value, the region with low Rothalpy value (wake region) is found. The wake can be found on suction side if $Ro < 1$ or on pressure side if $Ro > 1$. The Coriolis effect appears on the increase of the region of low radial velocity as the radius increase, the decrease in tangential pressure gradient at pressure side and the damping on turbulence intensity toward the pressure side and toward the impeller outlet as mentioned by Tuzson [22]. These phenomena are accurately predicted as shown in Fig 11.

All turbulence models predict the increase in wake region and the decrease in blade loading at this radius than previous one, Fig 10. Moreover, the radial velocity indicated by numerical simulation is close to the experimental data at this radius. The RSM and SST k-ω model indicate a difference in two measured passages in radial velocity component. RSM model reports that the recirculation continued strongly to this radius while SST k-ω model shows the different trend for radial velocity.

The change in flow properties near the impeller exit is illustrated at points with large radius shown in Fig. 12. The relative tangential velocity and radial velocity become lower in suction side than pressure side. This gradient contracts the traditional one for relative velocity magnitude. Hamkins *et al.*[21] and Miner *et al.* [12] deduced that this is a remark to an inverse blade loading occurred at this radius. This means that the flow will give the energy to the blade. Due to the current distribution of velocity components, the relative velocity magnitude at the pressure side will be higher than its value on the suction side, as shown in Fig. 13-a and c. This phenomenon is called jet – wake phenomenon.

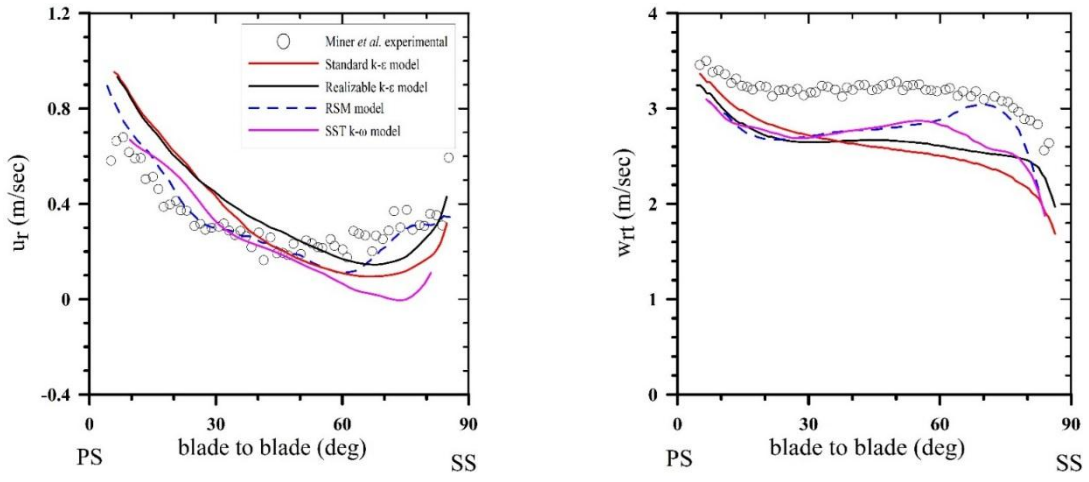

(a) $\theta = \pi$.

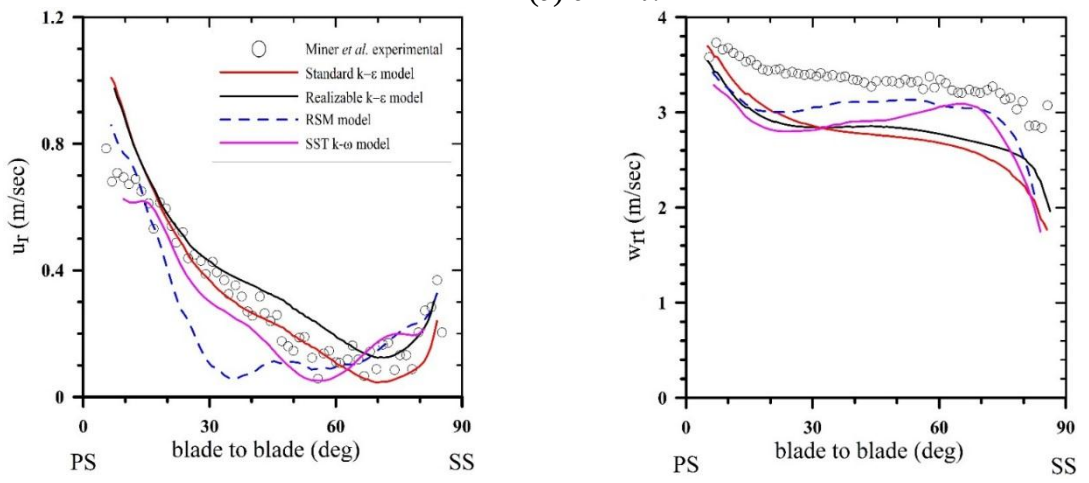

(b) $\theta = 0$.

Fig. 12. Radial and relative tangential velocity at $\boldsymbol{r = 100.3}$ mm and $\boldsymbol{z = 12.3}$ mm.

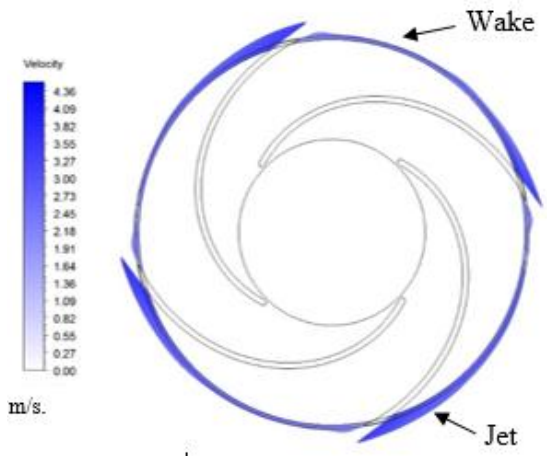

(a) Relative velocity at impeller exit.

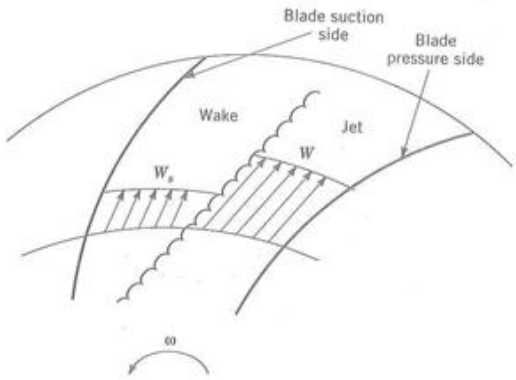

(b) Characteristic of jet-wake Ref. [22].

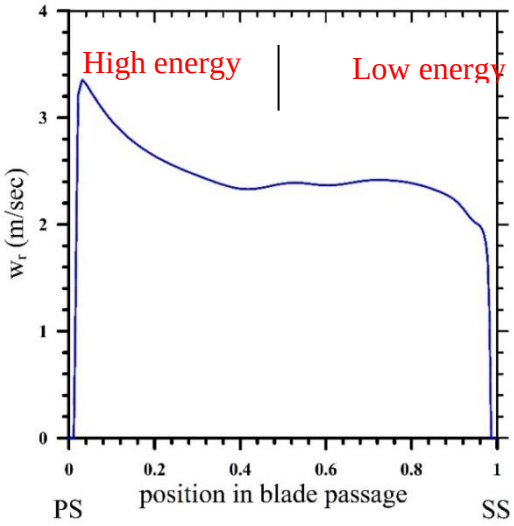

(c) Relative velocity at the exit of impeller passage.

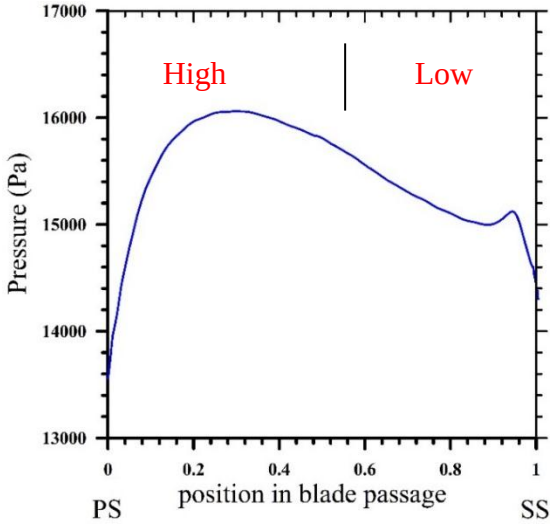

(d) Pressure at the exit of impeller passage.

Fig. 13. Jet – wake phenomenon.

Due to heavy blade loading, separation will occur at the pressure side. So, the maximum pressure value doesn't exist at blade surface as shown in Fig. 13. Since the separation cannot be stable on pressure side because of the rotation effect, the energy transfer to the fluid at blade pressure side making its relative velocity magnitude is high as conformity to relative energy equation, Fig. 13. On the other hand, the flow has different characteristics near both sides. Consequently, the flow pattern is divided into two fluid zones with different energy values separated by stabilized shear layer as shown in Figs. 13-b, c and d.

All tested turbulence models shown in Fig. 12, predict qualitatively this phenomenon. The radial velocity can be predicted fairly well by all the tested models. Although, The RSM model gives approximately the best results for radial velocity at $\theta = \pi$, it fails in the other side($\theta = 0$). Otherwise, the realizable k-ε model gives the closest trend for the relative tangential velocity to the measured data but with lower values. The worst trend is obtained for tangential component when the RSM and SST k-ω models are used.

From the previous results, it is clear that the turbulence models vary in their prediction results. One model gives better prediction at some points and another gives better at different points. A statistical analysis is needed to determine the most accurate turbulence model which gives the mean predicted results closer to the measured ones.

The Mean Deviation Error (MDE) between predicted and experimental results for the tested turbulence models is calculated by $MDE = \frac{1}{n}\sum_{i=1}^{i=n} abs(\frac{U_{num}-U_{exp}}{U_{exp}})$. The value of U_{num} and U_{exp} should be at the same angle. The statistical deviation results of radial velocity at six measuring points for each turbulence model are shown in Table 2. The results demonstrate that, the standard k-ε model predicts results with the smallest deviation and the largest deviation is given by RSM.

Table 2 Mean deviation of radial velocity for the tested turbulence models.

	Realizable k-ε	Standard k-ε	RSM	SST k-ω
$\theta = \Pi, r = 63.5$ mm	0.70296	0.4604098	0.6649941	0.6914912
$\theta = \Pi, r = 88.9$ mm	0.8100544	0.8991448	0.8705336	0.6500401
$\theta = \Pi, r = 100.3$ mm	0.3743999	0.4343802	0.1971344	0.4317752
$\theta = 0, r = 63.5$ mm	1.044543	0.521017	1.200321	0.9146816
$\theta = 0, r = 88.9$ mm	0.4010624	0.4569414	1.069166	0.5832472
$\theta = 0, r = 100.3$ mm	0.3663793	0.2691941	0.4218164	0.3333725
The mean deviation	0.6165665	0.506847883	0.737327583	0.600767967

Although the numerical and experimental results agree in predicting the inlet recirculation at $r = 63.5$ mm and $\theta = \pi$ and disagree in the difference between the two measured passages, the deviation between results at this measured point is larger than the other one as illustrated in Table 2. The deviation is enhanced for the next radius at the same angle for all turbulence models except RSM model. It is noticed that the minimum deviation for all turbulence models occurs at the outer measured points. The lowest deviation in the outlet diameter indicates that the eddy formed in the impeller decays and the flow becomes most likely isotropic flow.

Table 3 presents the mean deviation error of relative tangential velocity for the tested turbulence models. All turbulence models predict the relative tangential velocity better than radial velocity with respect to the mean deviation value. This reflects the ability of turbulence models to predict the secondary flow well. The RSM models gives the best solution results for the relative tangential velocity. The competition between different turbulence models is very hard regarding to the values of the mean deviation for them.

Table 3 Mean deviation of relative tangential velocity for the tested turbulence models.

	Realizable k-ε	Standard k-ε	RSM	SST k-ω
$\theta = \Pi, r = 63.5$ mm	0.1360527	0.158	0.1399036	0.2333062
$\theta = \Pi,\ r = 88.9$ mm	0.2153055	0.1780096	0.237843	0.2297148
$\theta = \Pi,\ r = 100.3$ mm	0.160	0.1745773	0.126433	0.145
$\theta = 0,\ r = 63.5$ mm	0.2783634	0.3242	0.2464532	0.2293809
$\theta = 0, r = 88.9$ mm	0.2171565	0.1936486	0.2156982	0.2794975
$\theta = 0,\ r = 100.3$ mm	0.154	0.1734244	0.106	0.1463752
The mean deviation	0.193524867	0.200286417	0.178790233	0.210593317

Tables 2 and 3 show that, the standard k-ε model is the best in predicting radial velocity. However, RSM is the best one for predicting the relative tangential velocity. Therefore, the mean deviation for the velocity components should to be calculated. Table 4 shows the mean deviation error for both velocity components. The results in this table show that the lowest mean deviation is given by standard k-ε model.

Table 4. Total mean deviation for each tested turbulence model.

	Realizable k-ε	Standard k-ε	RSM	SST k-ω
Total mean deviation	0.405045683	0.35356715	0.458058908	0.405680642

Although, RSM and SST k-ω models don't indicate the minimum value for the total deviation and take more time in calculation, they represent physical phenomenon which doesn't represented by the others. Actually, the flow velocity components at any point in pump domain, especially impeller domain, don't have a periodic value with time because of the generation and damping of different scale eddies depend on eddy life time. Consequently, the turbulence inside pump domain is very high. Only, the two mentioned turbulence models indicate that physical phenomenon, but with high calculation time, as illustrated from the value of measured quantities for complete revolution in Fig.14.

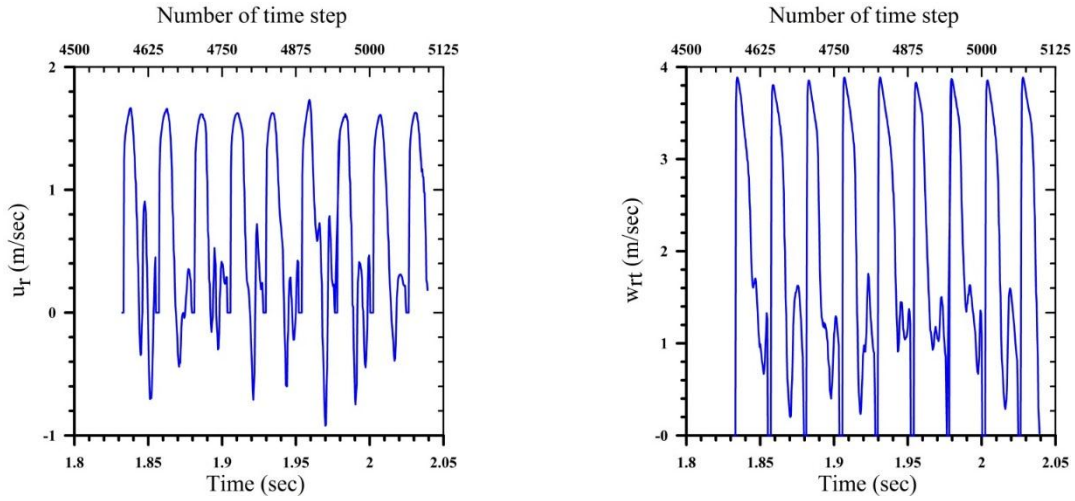

(a) RSM result for at $r = 63.5$ mm and $\theta = \pi$.

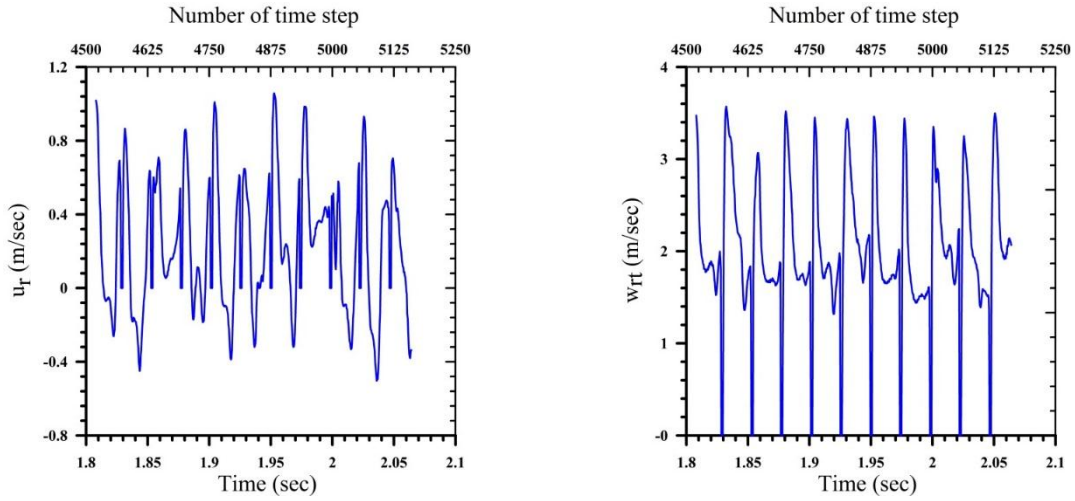

(b) SST k-ω for point at $r = 88.9$ mm and $\theta = 0$.

Fig. 14. Time history of velocity component.

6. Conclusion

The effect of turbulence modeling on the flow behavior in centrifugal pump was investigated using ANSYS FLUENT 15. Sliding mesh technique was used to solve the unsteady Reynolds average Navier-Stokes equations in three-dimensional domain. Four turbulence models were used to predict the flow turbulence. The predicted results were compared with experimental data from literature and satisfactory results were obtained. The results indicated that the time step used in the simulation must be less that the time required by the blade thickness to pass certain point at the outer periphery. In addition, it was found that none of the tested turbulence models can predict the flow behavior at location inside the pump. Statistical analysis based on mean square error, MDE showed that, the Standard $k-\varepsilon$ can predict better results than other tested models. In general, the current method can predict the physical phenomena such as inlet recirculation, jet-wake and blade loading with acceptable accuracy

7. References

[1] S. M. Selim, M. A. Hosien, S. M. El-Behery, and M. Elsherbiny, "Numerical analysis of turbulent flow in centrifugal pump," in 17th International Conference on Applied Mechanics and Mechanical Engineering., 2016, pp. 224–240.

[2] J. González, J. Fernández, E. Blanco, and C. Santolaria, "Numerical simulation of the dynamic effects due to impeller-volute interaction in a centrifugal pump," J. Fluids Eng., vol. 124, no. 2, pp. 348–355, 2002.

[3] M. Mentzos, A. Filios, P. Margaris, and D. Papanikas, "CFD predictions of flow through a centrifugal pump impeller," in Proceedings of International Conf. Experiments/Process/System Modelling/Simulation/Optimization. Athens, 2005.

[4] R. Barrio, J. Parrondo, and E. Blanco, "Numerical analysis of the unsteady flow in the near-tongue region in a volute-type centrifugal pump for different operating points," Comput. Fluids, vol. 39, no. 5, pp. 859–870, 2010.

[5] F. J. Silva, J. C. Páscoa, and J. S. Pinheiro, "Turbulent flowstructure computation inside a pump-PAT using an industrial benchmark test case," in European conference on computational fluid dynamics, 2010.

[6] A. Nocente, T. Arslan, D. Jasinski, and T. K. Nielsen, "A study of flow inside a centrifugal pump: high performance numerical simulations using GPU cards," in ISROMAC, 2016, pp. 1–7.

[7] S. Chakraborty and K. M. Pandey, "Numerical studies on effects of blade number variations on performance of centrifugal pumps at 4000 RPM," Int. J. Eng. Technol., vol. 3, no. 4, p. 410, 2011.

[8] W. Yulin, L. Shuhong, and S. Jie, "Numerical simulation on the steady and unsteady internal flows of a centrifugal pump," in Examples and Applications in Computational Fluid Dynamics, Prof. Lutz Angermann (Ed.), 2010, p. 440.

[9] H. Liu, X. Wu, and M. Tan, "Numerical investigation of the inner flow in a centrifugal pump at the shut-off condition," J. Theor. Appl. Mech., vol. 51, 2013.

[10] R. W. Westra, L. Broersma, K. Van Andel, and N. P. Kruyt, "PIV measurements and CFD computations of secondary flow in a centrifugal pump impeller," J. Fluids Eng., vol. 132, no. 6, p. 061104, 2010.

[11] S. M. El-Behery and M. H. Hamed, "A comparative study of turbulence models performance for separating flow in a planar asymmetric diffuser," Comput. Fluids, 2011, vol. 44, no. 1, pp. 248–257, 2011.

[12] S. M. Miner, R. J. Beaudoin, and Flack R.D., "Laser velocimeter measurements in a centrifugal flow pump," J. Turbomach. , vol. 111, no. 3, pp. 205–212, 1989.

[13] FLUENT 15 theory guide. ANSYS Inc., 2013.

[14] B. E. Launder and D. B. Spalding, “Mathematical Models of Turbulence.” Lecture notes, Imperial College of Science and Technology, 1972.
[15] B. E. Launder and D. B. Spalding, “The numerical computation of turbulent flows,” Comput. methods Appl. Mech. Eng., vol. 3, no. 2, pp. 269–289, 1974.
[16] T. H. Shih, W. W. Liou, A. Shabbir, Z. Yang, and J. Zhu, “A new k-ϵ eddy viscosity model for high Reynolds number turbulent flows,” Comput. Fluids, vol. 24, no. 3, pp. 227–238, 1995.
[17] F. R. Menter, “Two-equation eddy-viscosity turbulence models for engineering applications,” AIAA journal, vol. 32, no. 8, pp. 1598–1605, 1994.
[18] K. C. Thin, M. M. Khaing, and K. M. Aye, “Design and performance analysis of centrifugal pump,” world Acad. Sci. Eng. Technol., vol. 46, pp. 422–429, 2008.
[19] T. Z. Farge and M. W. Johnson, “Effect of flow rate on loss mechanisms in a backswept centrifugal impeller,” Int. J. heat fluid flow, vol. 13, no. 2, pp. 189–196, 1992.
[20] M. Abramian and J. H. G. Howard, “Experimental investigation of the steady and unsteady relative flow in a model centrifugal impeller passage,” J. Turbomach., vol. 116, no. 2, pp. 269–279, 1994.
[21] C. P. Hamkins and R. D. Flack, “Laser velocimeter measurements in shrouded and unshrouded radial flow pump impellers,” J. Turbomach., vol. 109, no. 1, pp. 70–76, 1987.
[22] J. Tuzson, Centrifugal Pump Design. John Wiley & Sons, inc., 2000.
[23] T. Elholm, E. Ayder, and R. Van den Braembussche, “Experimental study of the swirling flow in the volute of a centrifugal pump,” ASME 1990 Int. Gas Turbine Aeroengine Congr. Expo. Am. Soc. Mech. Eng., 1990.
[24] N. Pedersen, P. S. Larsen, and C. B. Jacobsen, “Flow in a centrifugal pump impeller at design and off-design conditions—part I: particle image velocimetry (PIV) and laser Doppler velocimetry (LDV) measurements,” J. Fluids Eng., vol. 125, no. 1, pp. 61–72, 2003.
[25] D. Adler and Y. Levy, “A laser-Doppler investigation of the flow inside a backswept, closed, centrifugal impeller,” J. Mech. Eng. Sci., vol. 21, no. 1, pp. 1–6, 1979.
[26] R. Dong, S. Chu, and J. Katz, “Effect of modification to tongue and impeller geometry on unsteady flow, pressure fluctuations, and noise in a centrifugal pump,” J. Turbomach., vol. 119, no. 3, pp. 506–515, 1997.